International Journal on Science and Technology (IJSAT)
E-ISSN: 2229-7677 ● Website: www.ijsat.org ● Email: editor@ijsat.org

Applications of Spectroscopic Techniques in Characterization of Biological Compounds

Ankur Malik

Department of Chemistry, Pt. Jawaharlal Nehru College, Banda-210001, (Affiliated to Bundelkhand University, Jhansi) India

ABSTRACT

Spectroscopic techniques are employed in analytical chemistry, biological analysis, and medicine. As technology has advanced, they have also been incorporated into other methods of analysis and estimation, such as elemental analysis, chromatography, and other identification tools. Microbes like cyanobacteria, the ancient oxygen-evolving photoautotrophs, have the ability to synthesize a wide variety of secondary metabolites and natural chemicals, according to advances in genome sequencing. When a secondary metabolite is produced in significant amounts, traditional structural elucidation and isolation procedures are reliable and effective; nevertheless, innovative methods are required for tiny quantities. High-performance liquid chromatography (HPLC), Fourier transform infrared spectroscopy (FTIR), electrospray ionization mass spectrometry (ESI-MS), Raman spectroscopy, and nuclear magnetic resonance spectroscopy (NMR) are the main methods used to investigate microbial and herbal secondary metabolites. Pre-separation of the metabolic components is necessary for MS and can be accomplished using analytical methods like GC or LC. Although specialized methods such arrayed electrochemical detection and FTIR have been employed in a number of situations, they also have distinct drawbacks. These days, metabolite identification from cell extracts or materials is typically done using HPLC and MS. For both pure chemicals and complicated combinations, NMR spectroscopy provides comprehensive information on molecular structure. Spectroscopy can identify these multifunctional molecules by providing additional information from the experimental data obtained for the characterization of secondary metabolites. Several recent developments in the characterization of microbial secondary metabolites using a variety of spectroscopic techniques, including UV-VIS spectroscopy, ESI-MS, FTIR, Raman spectroscopy, and NMR, are summarized in this work.

List of Abbreviations

HPLC: High-performance liquid chromatography

MS: Liquid chromatography/mass spectrometry

ESI-MS: Electrospray ionization mass spectrometry

FTIR: Fourier transform infrared spectroscopy

RT: Retention time

MALDI: Matrix-assisted laser desorption/ionisation

NMR: Nuclear magnetic resonance spectroscopy

INTRODUCTION

Through the application of chemometric techniques to foliar optical data, spectroscopy has recently emerged as an efficient way for precisely characterizing leaf biochemistry in living tissue; nevertheless, this approach has not been widely applied for plant secondary metabolites. The targeted metabolome technique, which may be utilized to offer thorough and simultaneous systematic profiling of metabolite levels in biofluids and tissues, allows for the quantification of limited collections of metabolites. Metabolites found in bodily fluids were mostly examined using NMR and MS prior to the introduction of various "omics" technologies, and multivariate statistics were used to interpret these complicated data sets. Pre-separation of metabolic components is necessary for MS, and this can be accomplished using analytical methods like GC/LC or its more sophisticated version, ultrahigh pressure LC (UPLC).Although specialized methods like FTIR and arrayed electrochemical detection have been employed in a number of situations, their application is constrained by the lack of precise molecular identification. These days, metabolite identification from cell extracts or materials is typically done using HPLC and MS. For both pure compounds and complex mixtures, NMR spectroscopy provides comprehensive information on molecular structure. However, metabolite molecular dynamics and mobility can also be investigated by interpreting NMR spin-relaxation durations and calculating molecular diffusion coefficients.

The most primitive group of Gram-negative photosynthetic oxygen-evolving prokaryotes are microbes like cyanobacteria, which most likely first appeared on Earth during the Precambrian era (between 2.8 and 3.5 billion years ago) when the ozone shield was absent (Tomitani et al. 2006), providing an oxygenic environment for the evolution of existing life forms (Fischer 2008). Due to their critical function in the photoprotection of microbial cells, microbial secondary metabolites including scytonemins and mycosporine-like amino acids (MAAs) are well-known UV-screening substances (Rastogi et al. 2010a). Tyrosine and tryptophan derivatives are likely involved in the formation of the pharmacologically significant secondary metabolite scytonemin (Proteau et al. 1993), and the gene cluster that produces scytonemin has been identified in certain cyanobacterial lineages (Balskus et al. 2011; Balskus and Walsh 2008, 2009; Sorrels et al. 2009; Soule et al. 2007, 2009). While secondary bioactive compounds from microbes have been analyzed using a variety of analytical techniques, secondary metabolites like MAAs (Whitehead and Hedges 2002) and scytonemin (Squier et al. 2004) have been extensively analyzed using high-performance liquid chromatography (HPLC) and mass spectrometry (MS). Both the lipid and carotenoid alterations in isolated thylakoid membranes were monitored using chemical techniques and membrane dynamics characterization in order to disclose the structural characteristics. Noninvasive Fourier transform infrared (FTIR) spectroscopy was employed for the latter. Lipid structural order has been effectively studied using FTIR spectroscopy in both biological membranes (Moore & Mendelsohn 1994; Moore et al. 1995) and models (Mantsch & McElhaney 1991; Mendelsohn & Senak 1993).

In this regard, the lipid fatty-acyl chains' $\nu_{sym}CH_2$ band has primarily been utilized. More disordered lipid fatty-acyl chains in the membranes are linked to its shift toward higher frequencies. They have demonstrated that this band may be broken down into two components that correspond to either the

ordered (trans) or disordered (gauche) segments of the fatty-acyl chains (Kota et al. 1999). By using this method to comprehend the membrane dynamics of *Synechocystis* PCC 6803 and its mutant strains that lack lipid desaturation, they have demonstrated that the cells work to maintain a standard degree of membrane dynamics at various growth temperatures (Szalontai et al. 2000). A novel tryptophan-containing microcystin congener from *Microcystis* CAWBG11, MC-WA, was discovered by researchers (Puddick et al. 2013).

It was also observed that a microcystin with a structure resembling that of MC-WA but with an extra mass of 32 Da was present (MC-1014). Using liquid chromatrography-tandem mass spectrometry (LC-MS/MS), two more tryptophan-containing microcystins from *Microcystis* CAWBG11 were identified. Nuclear magnetic resonance (NMR) spectroscopic examination of the previously mentioned MC-1014 showed that it was a novel microcystin that contained the tryptophan oxidation product, Nfk. This validates the speculative identification of seven more microcystin analogs with the oxidized tryptophan residues Nfk, Oia, and Kyn by LC-MS/MS. In addition to investigating the nature of gloeocapsin and other photoprotective pigments found in cyanobacteria and lichens, such as scytonemin, parietin, chlorophyll, and carotenoids, which can be detected with Raman spectroscopy, research offers Raman microspectroscopy and chemical mapping of living cyanobacteria.

Studies have concentrated on endoliths and epiliths subjected to water scarcity, extreme temperature and salinity fluctuations, and direct solar radiation (Ercegovic´ 1932; Jaag 1945; Golubic 1967a, 1967b; Hoffmann 1986). Because Raman microspectroscopy is non-destructive and only requires a tiny sample size, its usage in biochemical and biological studies has grown (Edwards et al. 2004, 2005; Marshall et al. 2007; Bowden et al. 2010). Nevertheless, there aren't many publications on the direct use of Raman microspectroscopy in relation to UV radiation on cyanobacteria. Researchers have used Raman microspectroscopy to simultaneously evaluate the variation of antioxidant small molecules in a desert cyanobacterium *Nostoc* sp. in order to examine how and when the antioxidant molecules are expressed by UVB radiation in cyanobacteria.

An excellent foundation for the detection of this crucial bioindicator of extant or extinct life on the surface or subsurface of Mars is the identification of distinctive and characteristic Raman spectroscopic signatures of scytonemin in the presence of related molecular features arising from other bioorganics like trehalose, carotenoids, and chlorophyll (Edwards et al. 2013). Together with chlorophyll molecules, carotenoids-a unique family of more than 400 conjugated polyenes with C_{40} modified and unsubstituted/unsaturated carbon-carbon chains-are in charge of absorbing radiation, mostly in the visible portion of the electromagnetic spectrum (Hemley and Kohler 1977; Sufra et al. 1977; Hladik et al. 1982; Siefermann-Harms 1985; Schafer et al. 2005). Three distinctive bands are seen in the Raman spectra profile of these kinds of polyunsaturated chains at particular wavenumbers in the range of 1600 to 1000 cm^{-1}. These bands provide conclusive information for the Raman spectroscopy characterization of those pigments (Withnall et al. 2003; de Oliveira et al. 2010, 2011; Samek et al. 2011; Castiglioni et al. 2011).

CHARACTERIZATION OF MICROBIAL SECONDARY METABOLITES HPLC AND ESI-MS

A Shimadzu high performance liquid chromatography (HPLC) system with a photodiode array (PDA) detector (SPD-M10A VP), an Inertsil® ODS-3 RP-18 column (5 µm, 250 × 4 mm), and a guard (Inertsil ODS-3, 5 µm, 4.0 × 10 mm) is used to further analyze the partially purified secondary metabolites like MAAs and scytonemin. For scytonemin, the mobile phase consisted of solvent A (ultra-pure water) and solvent B (acetonitrile–methanol–tetrahydrofuran, 75:15:10, v/v). The elution was carried out at a flow

rate of 1.5 mL min. 0-15 minutes of linear rise from 10% solvent A to 100% solvent B and 15-30 minutes at 100% solvent B were used in the 30-minute gradient elution protocol.

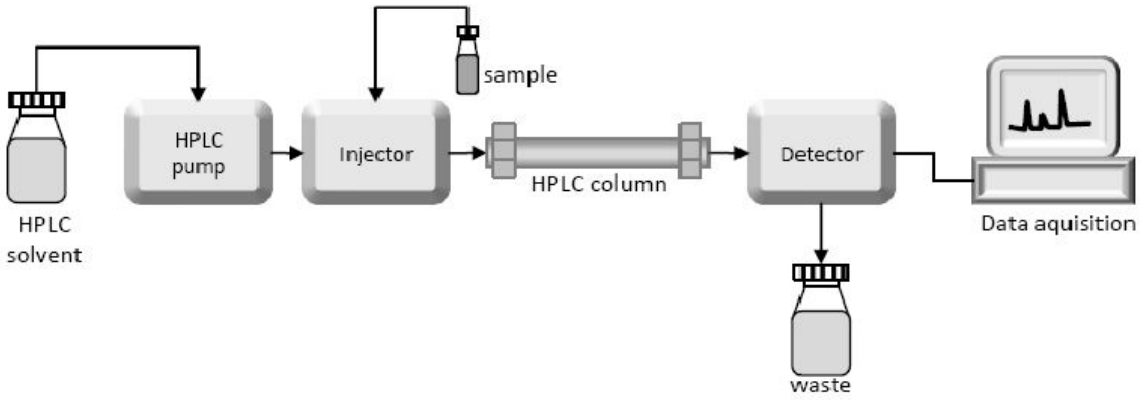

Figure 1: HPLC equipment consists of a pump, injector, column, detector, integrator, or acquisition and display system, as depicted in the schematic diagram above. The column where separation takes place is the central component of the system

The PDA scan wavelength ranged from 200 to 800 nm, while the detection wavelength was 380 nm. A series of trichromatic equations were used to measure the scytonemin concentration (Garcia-Pichel & Castenholz, 1991). The fraction containing pure scytonemin or its reduced counterpart (reduced scytonemin) was gathered and lyophilized (Sentry 2.0, VirTis, SP Scientific) after scytonemin absorption spectra were directly recorded every second on the HPLC separated peaks.

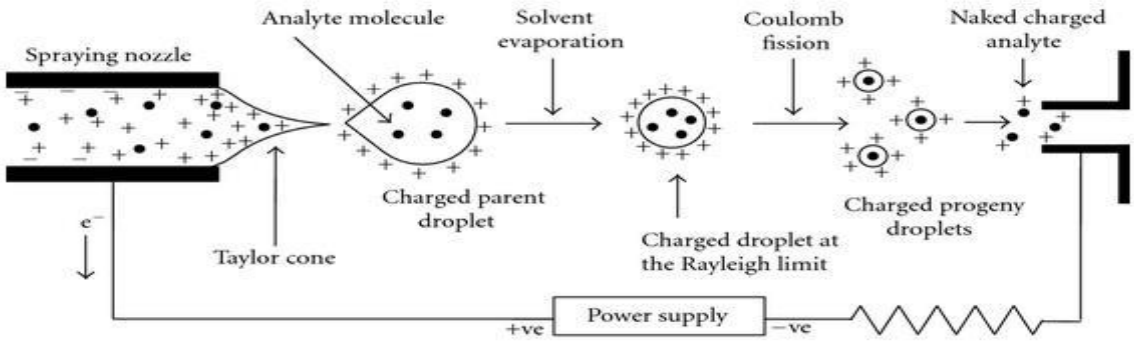

Figure 2: Schematic representation of the electrospray ionization process

Electrospray ionization mass spectrometry (ESI-MS) was used to further characterize the pure lyophilized scytonemin. With a scan range of m/z 200-700, the MS analysis was carried out in the positive electrospray ionization (ESI) mode. As previously mentioned, the pigment was identified using its mass and UV/Vis spectra (Squier et al. 2004).

FTIR SPECTROSCOPY

Membrane suspensions were resuspended in a D_2O-based 10 mM TES-NaOH pD 7.0 buffer after being centrifuged at 75,000 rpm for 20 minutes at 4°C in a Beckman TL100 centrifuge. (The movement of 0.4 units between pH and pD was considered.) This membrane suspension was positioned between CaF_2 windows, which were divided by an alumina spacer that was 25 mm thick. A Philips (Cambridge, UK) PU9800 FTIR spectrometer with a spectrum resolution of 2 cm^{-1} was used for the FTIR observations. 128 interferograms were gathered for every background and sample spectra.

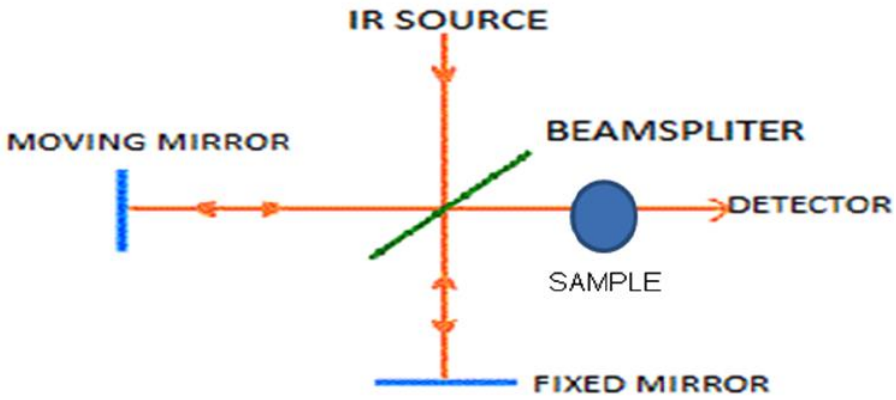

Figure 3: Schematic diagram about basics of FTIR

In order to perform temperature scans, the following measurement cycle was repeated: recording the sample and background spectra, waiting seven minutes, recording the sample and background spectra once more, setting a new temperature, and waiting seven minutes for the new thermal equilibrium to be formed. The results from the two spectra taken at the same temperature were averaged throughout the measurement evaluation. A water-thermostated sample holder was used to raise the temperature in steps of 2-3°C. The entire measuring cycle was managed by a computer. The temperature setting was more accurate than 0.5°C. SPSERV software (Cs. Bagyinka, Szeged, Hungary) was used to analyze the data. A linear baseline was removed from the spectra in the 2800-3050 cm^{-1} range prior to data analysis. There was no additional data modification (resolution enhancement, smoothing, etc.). Lorentzian component bands were used to fit the C-H stretching area of the spectrum utilizing two components for the fit of the $_{vsym}CH_2$ band, as previously reported (Kolta et al. 1999). The algorithm first freely optimized all of the component parameters (frequency, bandwidth, and intensity). The frequency and bandwidth of the stiff component were set for the temperature scan analysis that followed; the specifics are described in the text. The component band frequency determination was more accurate than 0.1 cm^{-1} (Vakonyi et al. 2002).

FTIR MEASUREMENTS IN THE PROTEIN CONFORMATION OF THE OXYGEN-EVOLVING CENTER IN CYANOBACTERIAL PHOTOSYSTEM II

PSII complexes (equivalent to 100 µg of chlorophyll) were suspended in a buffer containing 10 mM MES-NaOH (pH 6.0), 5 mM NaCl, and either 5 or 100 mM $CaCl_2$ in the presence of 30 mM potassium ferrocyanide and 20 mM potassium ferricyanide at a chlorophyll concentration of 0.05 mg mL^{-1}. The

complexes precipitated at 17000g for 15 minutes in the presence of 10% PEG6000. The final pellet was placed between two 25 mm-diameter CaF_2 plates. In order to preserve the non-heme iron in its reduced form, ferricyanide functions as an external electron acceptor and keeps the medium's redox potential relatively low (Noguchi and Inoue 1995). One of the CaF_2 plates features a circular groove with an inner diameter of 14 mm and a width of 1 mm. Silicone grease was applied to the outside of the groove to seal the sample cell. An aluminum foil piece of approximately 1 mm by 1 mm and 15 μm in thickness was positioned as a spacer in the cell's exterior. Cold water was circulated in a copper holder to get the sample temperature down to 10 °C. Before the spectra were taken, the sample was stabilized at this temperature in the dark for more than two hours. A Bruker IFS-66/S spectrophotometer fitted with an MCT detector (InfraRed D313-L) with 4 cm^{-1} resolution was used to acquire flash-induced S2/S1 FTIR difference spectra. A Q-switched Nd:YAG laser (Quanta-Ray GCR-130; 532 nm, ∼7 ns full width at half-maximum) with a power of ∼7 mJ $pulse^{-1}$ cm^{-2} at the sample point was used to illuminate flashes. To synchronize all centers to the S1 state, decrease the preoxidized non-heme iron to Fe^{2+}, and oxidize YD, the sample was exposed to two preflashes (1 Hz) and dark relaxation. Twice prior to and once following the illumination of a single flash, a single-beam spectrum (10 s scans) was captured. For samples (control, $^{+}$PsbO, $^{+}$PsbO/V, and $^{+}$PsbO/V/U) in the presence of 5 and 100 mM $CaCl_2$, respectively, the measurement was repeated 80 times with a dark interval of 10 and 12.5 minutes. A dark interval of 2.5 minutes was used for samples where all extrinsic proteins were depleted and only PsbV was restored due to significantly shorter relaxation times (15-25 s compared to 70-110 s in the control sample). An S2/S1 FTIR difference spectrum as after-minus-before illumination was computed using the averaged spectra. A baseline and a noise level are represented by the difference spectrum between the two spectra prior to illumination. To verify the intended composition of the extrinsic proteins in the PSII core complexes, PSII samples were taken out of the CaF_2 plates and submitted to SDS-PAGE following FTIR observations. Igor Pro (WaveMetrics Inc.) was used for spectral fitting. The fitting in the 1450-1350 cm^{-1} region (symmetric COO^{-} stretching vibrations) determined the variables used to normalize the spectra of treated PSII samples to those of untreated PSII (Uno et al. 2013). By deducting the normalized spectra from the spectrum of the untreated PSII, double-difference spectra were computed.

UV- VIS SPECTROSCOPY

A UV/Vis spectrophotometer (U-2910, 2J1-0012, Hitachi, Tokyo, Japan) was used to conduct spectroscopic examination for scytonemin and MAAs between 200 and 800 nm. Peaks were examined using the manufacturer's software after the raw data was moved to a microcomputer.

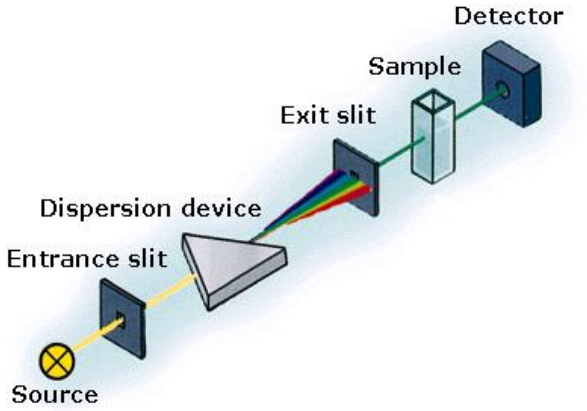

Figure 4: Schematic representation of UV-VIS spectrophotometry

NMR SPECTROSCOPY

For nuclear magnetic resonance (NMR) investigation, purified substances are dissolved in deuterium oxide (Cambridge Isotope Laboratories). A Bruker Avance III 600 MHz spectrometer with a cryogenic probe (operating at 600 MHz for 1H and 150 MHz for ^{13}C) locked to the deuterium signal is used to record one-dimensional (proton) and two-dimensional (correlation spectroscopy [COSY], heteronuclear multiple quantum correlation [HMQC], heteronuclear multiple-bond correlation [HMBC]) NMR spectra (Katoch et al. 2019).

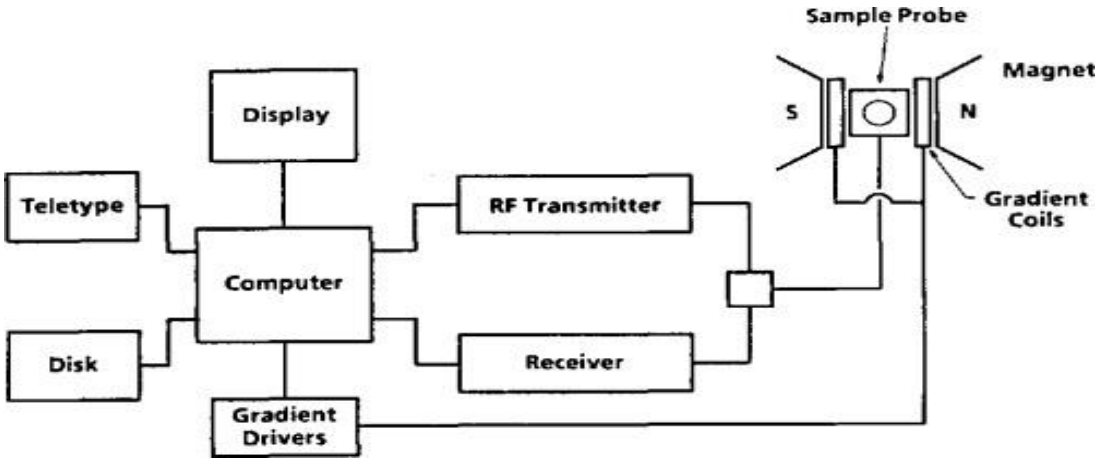

Figure 5: Simplified diagram of Nuclear Magnetic Resonance

Purple compound 1 ($C_{40}H_{34}N_2O_8$ by HRFABMS) showed two tertiary methyl groups resonating as singlets at approximately 2.95 and 3.15, a methine singlet at approximately 4.65, a typical AB system for a para substituted phenol with a hydroxyl proton at approximately 9.23, and signals for one disubstituted indole ring and an NH proton at approximately 12.12. A carbonyl signal at about 203.0, a

methine at approximately 85.3, a quaternary carbon at approximately 84.5, and two methoxy signals at approximately 52.4 and 56.6 were all visible in the ^{13}C NMR spectrum. An olefinic quaternary carbon signal at around 157.1 was detected among the aromatic carbons, suggesting a phenol function. The molecule's structural assignment was determined by 2D-NMR analysis. We were able to connect the para-substituted phenol to the CH-9 with a methoxy starting with the long-range correlations of H-11/H-15. HMBC correlations of H-9 with C-2, C-3 carrying O-CH3-17, C-3a, and C-10 were used to construct a second spin system. Long-range associations between H3-17 and C-3 and C-9 were observed. The long-range correlations found for H-4 with C-3a, C-4a, C-8a, and C-8b as well as the COSY and HMBC correlations of H-5 to H-8 established the disubstituted indole ring. The two dimeric units were connected by the remaining two quaternary carbons, C-1 and C-1¢. By examining molecular models, the geometry of the tetra substituted olefin in 1 was predicted to be E, and MM_2 computation verified that it was the lower isomer (Bultel-Ponce et al. 2003).

RAMAN SPECTROSCOPY

A Renishaw *via* Raman spectrometer connected to a Leic DM 2500 confocal microscope and an Ar-ion 50mW monochromatic 514.5 nm laser source was used for the Raman investigations. Laser excitation was focused through 50× (numerical aperture = 0.83) and 100× (numerical aperture = 0.74) objectives after being adjusted to an on sample intensity of maximum approximately 2mW (measured with a Coherent Laser Check analyzer). Acquisitions were made using an air-cooled (-70°C) 1024x256 pixel CCD array detector and a grating with 1800 grooves/mm. A spectral detection range of 2000 cm^{-1} was made possible by this technique. Every day, a Si-Al microprocessor chip with a distinctive Si Raman band at 520.5 cm^{-1} was used for beam centering and Raman spectra calibration. Wire 4.1 software was used to modify spectra. Static recording mode (fixed at 1150 cm^{-1}) was used for point and static line-scanning analytical measurements. The type and distribution of UV-protecting pigments were also identified using a high-resolution dynamic line-scanning Raman mapping technique (Renishaw HR Stream Line mode). The resulting map (4958 acquisitions) is a real hyperspectral mapping. The area covered by these photos is 96.2 x 87.1 lm (1.3 µm step). The measurement took 461 seconds in total. Fig. 6 displays Raman mapping pictures created at each sample point using the "intensity at point" mapping tool. The "through fixed point" fitting technique has been used to baseline correct the spectra. The chemical map is created without the use of interpolation modes (Jean-Yves Storme et al. 2015). The Pasteur suite on the upcoming ESA/IKI Roscomos ExoMars 2018 mission has recently embraced Raman spectroscopy as a first-pass analysis method to look for evidence of current or former life on Mars (Edwards et al. 2012). The ability of the Raman technique to distinguish non-destructively between bioorganic molecules and their inorganic host matrices (Edwards 2010) without requiring separation and treatment procedures will be the basis for an initial assessment of the planet's potential biohazards for human exploration. An excellent foundation for the detection of this crucial bioindicator of extant or extinct life on the surface or subsurface of Mars is the identification of distinctive and characteristic Raman spectroscopic signatures of scytonemin in the presence of related molecular features arising from other bioorganics like trehalose, carotenoids, and chlorophyll (Edwards et al. 2013).

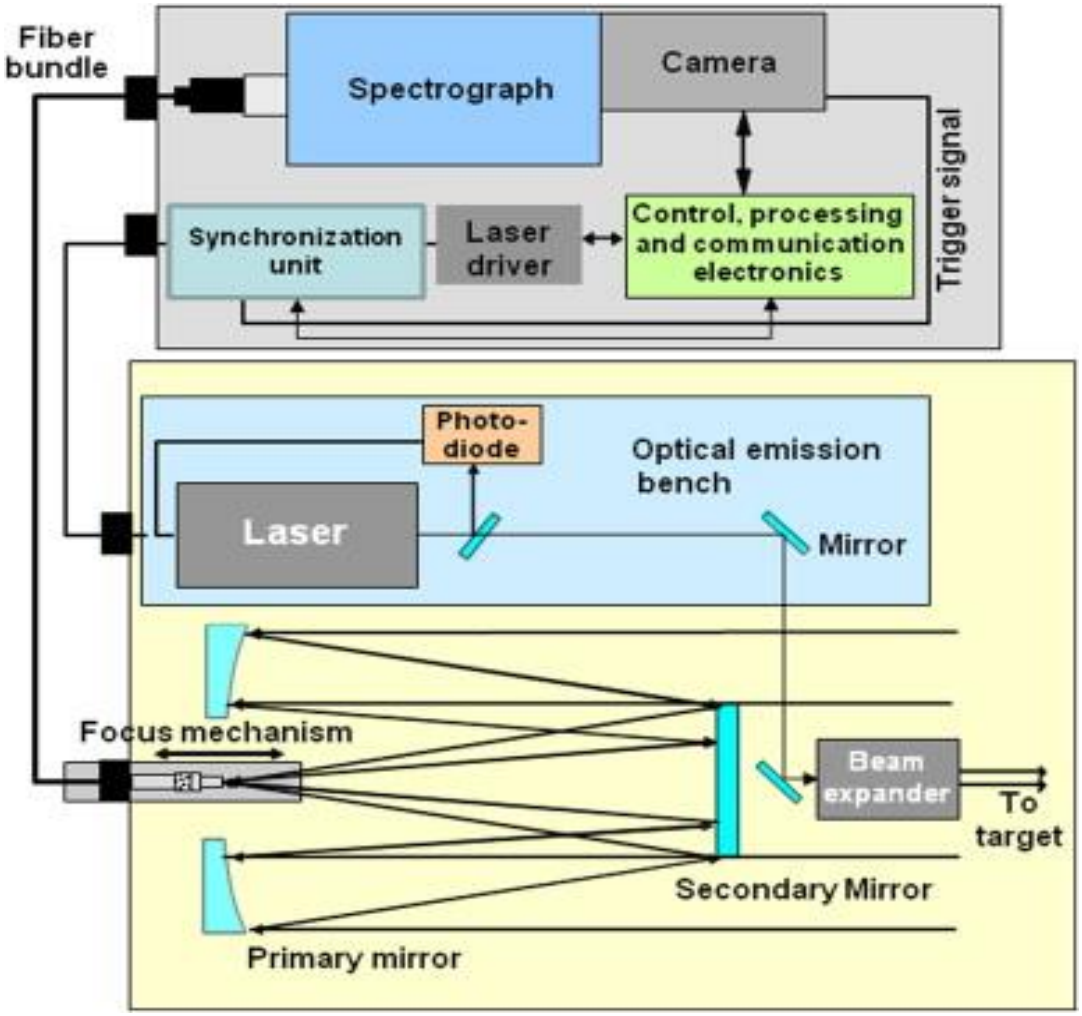

Figure 6: Block diagram of the UV stand-off Raman prototype developed by INO (Forest et al. 2012)

In this regard, the molecular modeling work and density functional theory (DFT) calculations of Varnali et al. (Varnali et al. 2009; Varnali and Edwards 2014) have been crucial in the interpretation of the experimental Raman spectral data, allowing for the dissection of the modes that make up the observed data signatures. A Raman spectrum's quality can be affected by a number of circumstances, which can make diagnostic interpretation challenging, particularly when comparing with a database and in the presence of possibly interfering biological components. The laser wavelength, wavenumber range, and spectral resolution are particularly crucial factors (Jorge-Villar and Edwards 2006).

RAMAN SPECTROSCOPIC PROTOCOL FOR THE PROPOSED STRUCTURES OF IRON COMPLEXES

A comparison of the predicted Raman spectrum with that observed experimentally for the parent scytonemin (Edwards et al. 2000) and an analysis of the theoretical data from density functional theory (DFT) calculations on the most stable energetically favored iron-scytonemin complex structure in Table 1 reveals that, although some aromatic phenyl skeletal modes show slight wavenumber changes, as might be expected for a rigid and highly conjugated aromatic ring substructure, the iron atom's η6–η2 coordination has caused a significant structural change in the co-relationship between the two halves of

the dimeric molecule, which now shows a marked asymmetry when compared to the parent scytonemin. As a result, new Raman bands predicted at 1767 and 1754 cm^{-1}, which appear to originate from decoupled carbonyl modes, have replaced the bands experimentally observed in scytonemin at 1656 and 1710 cm^{-1}, which were assigned to C=C and C=O modes, as confirmed by the DFT computational analysis. In contrast, the iron-scytonemin complex retains the unsaturated aromatic ring C=C mode in the parent scytonemin at 1605 cm^{-1}, which is attributed to the phenol ring C=C mode related to vinyl stretching at 1607 and 1605 cm^{-1}.

Table 1. Predicted major Raman bands (cm^{-1}) for iron complexes of scytonemin and its methoxy-derivatives (most active bands are bold).

scytonemin (cm^{-1})	**dimethoxyscytonemin (cm^{-1})**	**Tetramethoxyscytonemin one iron (cm^{-1})**	**two irons (cm^{-1})**
3595, 3579	3635, 3614	3621	3536, 3526
—	3486, 3450	3468, 3451	3357, 3354
3075, 3042	3107, 3089	3103, 3075	3102, 3099
3035	3044	—	3090, 3086
—	2944, 3067	2943, 3063	**2959, 2953**
—	2898	2897	2919
1767, 1754	1761	1751	—
1607, **1605**	1607	—	—
1591	1585	1584	1593
1557	1558	**1552**	**1572, 1567**
1547	—	—	1540
—	**1538**, 1527	1525	—
1497, 1489	—	—	—
1475, **1470**	**1469**, 1467	**1467**	1478
—	1456	**1450**	—
—	1444	—	**1434**, 1421
1431, 1425	1416, 1411	1412	1415, 1404
1380, 1370, 1338	1387, 1377, 1364, 1357	1383, 1360	—
	1348, 1338, 1335, 1321	**1335**, 1312	1327

—	1289	—	**1297**
1277	1263	—	—
1176	1185, 1168, 1146	1198, 1173	—
—	1130, 1105	**1142**	1119
1075	**1076**	1074	**1081**
1064, 1061	—	**1047**	**1054**

The iron complex still has a second weak band at 1557 cm^{-1}, which is attributed to the stretching of the sequence $C_2=C_1–C_{22}=C_{33}$ between the two halves of the molecule, which is now in the *cis* conformation. The experimentally observed most active band of scytonemin at 1590 cm^{-1}, which was theoretically assigned to the trans double bond ($C_2=C_1–C_{22}=C_{33}$), vinyl stretching, and coupled aromatic quadrant modes. In the iron–scytonemin complex, the aromatic ring C=C and C−N linked mode at 1525 cm^{-1} in scytonemin is now considerably displaced to 1547 cm^{-1}. The iron complex now exhibits strong C-O bands at around 1497 and 1489 cm^{-1}, which originate from the previously described decoupled CO modes. Theoretically, the conversion of parent scytonemin to an iron-scytonemin complex is expected to have little effect on other vibrational modes. For example, the bands at 1375 and 1384 cm^{-1} in scytonemin are found at 1370 and 1380 cm^{-1} in the complex, as are the bands at 1323, 1283, and 1245 cm^{-1}, which are now also found at 1338 and 1277 cm^{-1} with a doublet feature at 1231/1249 cm^{-1}. In scytonemin, the doublet at 1102 and 1090 cm^{-1} now occurs at 1100 and 1075 cm^{-1}. It is anticipated that the complex's bands at 1075 and 1176 cm^{-1} will be highly active. There are now additional bands at 978, 913, and 748 cm^{-1} instead of 984, 889, 835, and 754 cm^{-1}. The Raman spectra of the parent scytonemin and its iron complex differ rather noticeably, which may serve as the foundation for their distinction, even though some of these wavenumber differences are expected to be negligible. For the scytonemin/iron–scytonemin complex, lower frequency modes like 677/689, 565/560, 539/535, 500/497, 450/435, and 274/280 cm^{-1} are also expected to have a number of commonalities. In conclusion, the complexation of iron(III) with its location across the two extreme aromatic ring systems of scytonemin has theoretically produced a new structure that should be detectable experimentally in the Raman spectrum. This could allow for the experimental detection of the spectral signatures of a scytonemin–iron complex produced by extremophilic cyanobacterial colonies in iron-rich geological environments. According to the theoretical study, the key spectral wavenumber region, 1400-1800 cm^{-1}, where several of the major differences appear for discriminatory purposes, must be the focus of the predicted Raman spectroscopic differentiation between the parent scytonemin and a potential iron-scytonemin complex that could be formed by cyanobacterial colonization in iron-rich geological scenarios. Specifically, the identification of this complexation will depend on the replacement of the important scytonemin characteristics at 1710 and 1656 by the novel doublets resulting from the structurally decoupled carbonyls at 1767 and 1754 cm^{-1} and 1497, 1489 cm^{-1}. The presence of iron-scytonemin complexation in future experimentally recorded spectra would also be supported by confirmation from the shifted parent scytonemin band at 1525-1547 cm^{-1}. The single OH and NH bands each become two bands for the complex, according to a thorough comparison of the data for the methoxy derivatives and their iron complexes. Because one of the carbonyls is involved in the complexing to the iron, the two carbonyl bands found in the methoxy derivatives (1710, 1729 cm^{-1} for

dimethoxy and 1721, 1733 cm^{-1} for tetramethoxy) now appear at higher wavenumbers as just one band in the complexes (1761 cm^{-1} for dimethoxy and 1751 cm^{-1} for tetramethoxy). There is no discernible carbonyl band in the diiron complex if both carbonyl groups are involved in complexation. For the iron-dimethoxyscytonemin complex, the 1626 cm^{-1} band assigned to vinyl stretching becomes a band at 1607 cm^{-1}; for the one iron complex, the 1603 cm^{-1} band becomes the 1584 cm^{-1} band; and for the diiron complex, it becomes the 1593, 1572, and 1567 cm^{-1} bands. Dimethoxyscytonemin's 1547 cm^{-1} band (1550 cm^{-1} for tetramethoxyscytonemin) splits into two bands at 1538 and 1527 cm^{-1} (1552 and 1525 cm^{-1} for tetramethoxyscytonemin) for the one iron complex and at 1552 and 1540 cm^{-1} for the diiron complex. For the dimethoxy, tetramethoxyscytonemin one iron complex, and diiron complex, the 1474 cm^{-1} band changes to 1469 cm^{-1}, 1467 cm^{-1}, and 1478 cm^{-1}, respectively. Even though the computational study revealed some significant vibrational properties that could be verified by experimental Raman spectroscopy, the complex vibrations that occur below 1400 cm^{-1} cannot be attributed to individual idealized group motions due to significant mode coupling. Dimethoxyscytonemin's complex exhibits bands at 1387, 1377, 1364, 1357, 1335, and 1321 cm^{-1}, while its weak bands at 1338 and 1348 cm^{-1} get stronger. Along with other bands at 1383, 1362, 1357, 1320, and 1312 cm^{-1}, tetramethoxyscytonemin's 1336 cm^{-1} band becomes stronger and appears at 1335 cm^{-1}. The feature at 1327 cm^{-1} is the only active band for the combination with two iron atoms in this region. Since potential key molecules that could be produced by organisms in highly stressed environments have been identified but have not yet been observed experimentally in terrestrial Mars analogue scenarios, the theoretical analyses and predictions made in this paper have direct relevance to the upcoming ExoMars 2018 mission and subsequent missions to Mars. Before more destructive experimental techniques are planned, bio-signatures must be identified from a Raman database in order to conduct remote instrumental analytical interrogation of the Martian planetary surface and subsurface (Edwards 2010). Therefore, it is crucial that a variety of potential biosignatures be gathered on land (Vitek et al. 2012; Edwards et al. 2012). In order to make it easier to identify them in the biomolecular and mineral mixtures that are commonly found in biogeological matrices, predictions of the spectral activity of as-yet-undetermined Raman biosignature wavenumbers are crucial.

CONCLUSION

Microbial secondary metabolites are attractive targets in biotechnology and biomedical research because they have potential uses in industry, agriculture, and pharmaceuticals. Metabolomics complements transcriptomics, proteomics, and genomes at the metabolite level. Metabolomic analyses are the level most directly associated with the physiology of an organism, organ, or cell as compared to proteomics and transcriptomics. Comprehensive and standardized metabolite examinations of complicated biological materials are made possible by analytical methods like HPLC, ESI-MS, FTIR, MALDI-TOF, and NMR. Because of the metabolome's complex composition, which includes a wide range of quantities of highly different chemical compounds, it is extremely difficult to identify and quantify all cellular metabolites using the fragmentation pattern using MS. Therefore, current metabolome research is focused on improving analytical technology, experimental protocols, and data interpretation.

REFERENCE

1. Balskus, E.P., Walsh, C.T., 2008. Investigating the initial steps in the biosynthesis of cyanobacterial sunscreen scytonemin. J. Am. Chem. Soc. 130, 15260–15261.
2. Balskus, E.P., Walsh, C.T., 2009. An enzymatic cyclopentyl[b]indole formation involved in scytonemin biosynthesis. J. Am. Chem. Soc. 131, 14648–14649.
3. Balskus, E.P., Case, R.J., Walsh, C.T., 2011. The biosynthesis of cyanobacterial sunscreen scytonemin in intertidal microbial mat communities. FEMS Microbiol. Ecol. 77, 322–332.
4. Bowden, S.A., Wilson, R., Cooper, J.M., and Parnell, J. (2010) The use of surface-enhanced Raman scattering for detecting molecular evidence of life in rocks, sediments, and sedimentary deposits. Astrobiology 10:629–641.
5. Bultel-Ponce´, V., F. Felix-Theodose, C. Sarthou, J.-F. Ponge and B. Bodom 2003. New Pigments from the Terrestrial Cyanobacterium *Scytonema* sp. Collected on the Mitaraka Inselberg, French Guyana (doi:10.1007/s00216-005-0029-2).
6. Castiglioni, C., A. Milani, D. Fazzi, F. Negri, Modulation of the electronic structure of polyconjugated organic molecules by geometry relaxation: a discussion based on local Raman parameters, J. Mol. Struct. 993 (2011) 26–37.
7. de Oliveira V.E., Almeida, E.W.C., Castro, H.V., Edwards, H.G.M., Dos Santos, H.F., de Oliveira, L.F.C.Carotenoids and b-cyclodextrin inclusion complexes: Raman spectroscopy and theoretical investigation, J. Phys. Chem. A 115 (2011) 8511– 8519.
8. de Oliveira, V.E., Castro, H.V., Edwards, H.G.M., de Oliveira, L.F.C. Carotenes and carotenoids in natural biological samples: a Raman spectroscopic analysis, J. Raman Spectrosc. 41 (2010) 642–650.
9. Edwards HGM, Garcia-Pichel F, Newton EM, Wyn-Williams DD. 2000 Vibrational Raman spectroscopic study of scytonemin, the UV-protective cyanobacterial pigment. *Spectrochim. Acta A* 56, 193–200. (doi:10.1016/S1386-1425(99)00218-8).
10. Edwards HGM, Hutchinson IB, Ingley R. 2012 Raman spectroscopy and the search for life signatures in the ExoMars mission. *Int. J. Astrobiol.* **11**, 269–278. (doi:10.1017/m S1473550412000201)
11. Edwards HGM, Hutchinson IB, Ingley R. 2012 The Raman Spectrometer on the ExoMars mission and the identification of spectroscopic signatures: a biogeological perspective. *Anal. Bioanal. Chem.* **404**, 1723–1731. (doi:10.1007/s00216-012-6285-z)
12. Edwards HGM, Hutchinson IB, Ingley R. 2013 Raman spectral signatures in the biogeological record: an astrobiological challenge. In *Habitability on other planets and satellites: the quest for extraterrestrial life. Part VI: applications of existing technologies for the detection of habitable planets and the search for life*, vol. 22 (eds JP de Vera, J Seckbach), pp. 311–330. Berlin, Germany: Springer.
13. Edwards HGM, Hutchinson IB, Ingley R. 2013 Raman spectral signatures in the biogeological Edwards HGM. 2010 Analytical astrobiology: the role of Raman spectroscopy in biomarker speciation for extraterrestrial life detection. In *Astrobiology: emergence, search and detection of life* (ed. VA Basiuk), pp. 361–375. Stevenson Ranch, CA: American Scientific Publishers.
14. Edwards HGM. 2010 Raman spectroscopic approach to analytical astrobiology: the detection of key geological and biomolecular markers in the search for life. *Phil. Trans. R. Soc. A* **368**, 3059–3066. (doi:10.1098/rsta.2010.0100)
15. Edwards, H.G.M., Moody, C.A., Villar, S.E.J., and Mancinelli, R. (2004) Raman spectroscopy of desert varnishes and their rock substrata. J Raman Spectrosc 35:475–479.

16. Edwards, H.G.M., Moody, C.D., Newton, E.M., Villar, S.E.J., and Russell, M.J. (2005) Raman spectroscopic analysis of cyanobacterial colonization of hydromagnesite, a putative martian extremophile. Icarus 175:372–381.
17. Ercegovic´, A. (1932) Ekolos˘ke isociolos˘ke studije o litofitskim cijanoficejama sa jugoslavenske obale Jadrana. Rad Jugosl Akad Znan Umjet Razred Med Znan 244:129–220.
18. Fischer WF (2008) Life before the rise of oxygen. *Nature* 455: 1051–1052
19. Gaohong Wang, Zongjie Hao, Zebo Huang, Lanzhou Chen, Xiaoyan Li, Chunxiang Hu, and Yongding Liu 2010. Raman Spectroscopic Analysis of a Desert Cyanobacterium *Nostoc* sp. in Response to UVB Radiation (doi: 10.1089/ast.2009.0407).
20. Golubic, S. (1967a) Algenvegetation der Felsen. Eine O¨ kologische Algenstudieimdinarischen Karstgebiet. In Die Binnengewa¨sser, edited by H.J. Elster and W. Ohle, Schweizerbart'sche Verlagsbuchhandlung, Stuttgart, 23:1–183.
21. Golubic, S. (1967b) Die Algenvegetation an Sandsteinfelsen Ost-Venezuelas (Cumana). Int Rev Hydrobiol 52:693–699.
22. Hemley, R.K., B.E. Kohler, Electronic structure of polyenes related to the visual chromophore. A simple model for the observed band shapes, Biophys. J. 20 (1977) 377–382.
23. Hladik, J., P. Pancoska, D. Sofrova, The influence of carotenoids on the conformation of chlorophyll-protein complexes isolated from the cyanobacterium Plectonema boryanum. Absorption and circular dichroism study, Biochim. Biophys. Acta – Bioenerg. 681 (1982) 263–272.
24. Hoffmann, L. (1986) Cyanophyce´es ae´riennes et subae´riennes du Grand-Duche´ de Luxembourg. Bulletin du Jardin botanique national de Belgique 56:77–127.
25. Jaag, O. (1945) Untersuchungen u¨ber di Vegetation und Biologie der Algen des nackten Gesteins in den Alpen, im Jura und im schweizerischen Mittelland. Beitra¨ge zur Kryptogamenflora der Schweiz 9:1–560.
26. Jorge-Villar SE, Edwards HGM. 2006 Raman spectroscopy in astrobiology. *Anal. Bioanal. Che* **384**, 100–113.
27. Katoch, M., Rabia Mazmouz, Rocky Chau, Leanne A. Pearson, Russell Pickford, Brett A. Neilan (2019) Heterologous Production of Cyanobacterial Mycosporine-Like Amino Acids Mycosporine- Ornithine and Mycosporine-Lysine in *Escherichia coli*.
28. Ko´ta, Z., Debreczeny, M. & Szalontai, B. (1999) *Biospectroscopy* **5,** 169–178.
29. Mantsch, H. H. & McElhaney, R. N. (1991) *Chem. Phys. Lipids* **57,** 213–226.
30. Marshall, C.P., Leuko, S., Coyle, C.M., Walter, M.R., Burns, B.P., and Neilan, B.A. (2007) Carotenoid analysis of halophilic archaea by resonance Raman spectroscopy. Astrobiology 7:631 643.
31. Mendelsohn, R. & Senak, L. (1993) in *Biomolecular Spectroscopy, Part A*, eds. Clark, R. J. H. & Hester, R. E. (Wiley, Chichester, U.K.), pp. 339–380.
32. Moore, D. J. & Mendelsohn, R. (1994) *Biochemistry* **33,** 4080–4085.
33. Moore, D. J., Sills, R. H. & Mendelsohn, R. (1995) *Biospectroscopy* **1,** 133–140.
34. Noguchi, T., and Inoue, Y. (1995) Identification of Fourier transform infrared signals from the non-heme iron in photosystem II. J. Biochem. 118, 9−12.
35. Proteau, P.J., Gerwick, W.H., Garcia-Pichel, F., Castenholz, R., 1993. The structure of scytonemin, an ultraviolet sunscreen pigment from the sheaths of cyanobacteria. Experientia 49, 825–829.
36. Puddick, J.; Prinsep, M.R.; Wood, S.A.; Cary, S.C.; Hamilton, D.P.; Wilkins, A.L. Isolation and structure determination of two new hydrophobic microcystins from Microcystis sp. (CAWBG11). Phytochem. Lett. 2013, doi:10.1016/j.phytol.2013.07.011.

37. Rastogi RP Richa Singh RP Singh SP Häder D-P (2010a) Photoprotective compounds from marine organisms. *J Ind Microbiol Biotechnol* 37: 537–558.
38. Samek, O., P. Zemanek, A. Jonas, H.H. Telle, Characterization of oil-producing microalgae using Raman spectroscopy, Laser Phys. Lett. 8 (2011) 701–709.
39. Schafer, L. Vioque, A. Sandmann G., Functional in situ evaluation of photosynthesis-protecting carotenoids in mutants of the cyanobacterium Synechocystis PCC6803, J. Photochem. Photobiol., B 78 (2005) 195–201.
40. Siefermann-Harms, D. Carotenoids in photosynthesis. I. Location in photosynthetic membranes and light-harvesting function, Biochim. Biophys. Acta-Bioenerg. 811 (1985) 325–355.
41. Sorrels, C.M., Proteau, P.J., Gerwick, W.H., 2009. Organization, evolution, and expression analysis of the biosynthetic gene cluster for scytonemin, a cyanobacterial UV absorbing pigment. Appl. Environ. Microbiol. 75, 4861–4869.
42. Soule, T., Stout, V., Swingley, W.D., Meeks, J.C., Garcia-Pichel, F., 2007. Molecular genetics and genomic analysis of scytonemin biosynthesis in *Nostoc punctiforme* ATCC 29133. J. Bacteriol. 189, 4465–4472.
43. Soule, T., Palmer, K., Gao, Q., Potrafka, R.M., Stout, V., Garcia-Pichel, F., 2009. A comparative genomics approach to understanding the biosynthesis of the sunscreen scytonemin in cyanobacteria. BMC Genomics 10, 336–345.
44. Squier, A.H., Airs, R.L., Hodgson, D.A., Keely, B.J., 2004. Atmospheric pressure chemical ionisation liquid chromatography/mass spectrometry of the ultraviolet screening pigment scytonemin: characteristic fragmentations. Rapid Commun. Mass Spectrom. 18, 2934–2938.
45. Storme, J-Y, Stjepko Golubic, Annick Wilmotte, Julia Kleinteich, David Vela´zquez, and Emmanuelle J. Javaux (2015) Raman Characterization of the UV-Protective Pigment Gloeocapsin and Its Role in the Survival of Cyanobacteria.
46. Sufra, S., G. Dellepiane, G. Masetti, G. Zerbi, Resonance Raman spectrum of bcarotene, J. Raman Spectrosc. 6 (1977) 267–272.
47. Szalontai, B., Nishiyama, Y., Gombos, Z. & Murata, N. (2000) *Biochim. Biophys. Acta* **1509,** 409–419.
48. Tomitani A Knoll AH Cavanaugh CM Ohno T (2006) The evolutionary diversification of cyanobacteria: molecular phylogenetic and paleontological perspectives. *P Nat Acad Sci USA* 103: 5442–5447.
49. Uno, C., Nagao, R., Suzuki, H., Tomo, T., and Noguchi, T. (2013) Structural coupling of extrinsic proteins with the oxygenevolving center in red algal photosystem II as revealed by light-induced FTIR difference spectroscopy. Biochemistry 52, 5705−5707.
50. Varnali T, Edwards HGM, Hargreaves MD. 2009 Scytonemin: molecular structural studies of a key extremophilic biomarker for astrobiology. *Int. J. Astrobiol.* **8** 133–140. (doi:10.1017/ S1473550409004455)
51. Varnali T, Edwards HGM. 2014 Reduced and oxidized scytonemin: theoretical protocol for Raman spectroscopic identification of potential key biomolecules for astrobiology. *Spectrochim. Acta A* **117**, 72–77. (doi:10.1016/j.saa.2013.08.002)
52. Vitek P, Jehlicka J, Edwards HGM, Hutchinson IB, Ascaso C, Wierzchos J. 2012 The miniaturised Raman system and detection of traces of life in halite from the Atacama desert: some considerations for the search for life signatures on Mars. *Astrobiology* **12**, 1095–1099. (doi:10.1089/ast.2012.0879)
53. Whitehead and Hedges (2002) Analysis of mycosporine-like amino acids in plankton by liquid chromatography electrospray ionization mass spectrometry. *Mar Chem* 80: 27–39.

54. Withnall, R., Chowdhry, B.Z., Silver, J., Edwards, H.G.M., de Oliveira, L.F.C. Raman spectra of carotenoids in natural products, Spectrochim. Acta Part A Mol. Biomol. Spectrosc. 59 (2003) 2207–2212.